Boletim da Sociedade Astronômica Brasileira, **37**, no. 1, 93-97

Sampling process to support an artificial intelligence approach for determining the structural parameters of open star clusters

Dener César Mendes[1], Valdivino Alexandre de Santiago Júnior[1] & Mateus de Souza Angelo[2]

[1] Laboratório de Inteligência ARtificial para Aplicações AeroEspaciais e Ambientais (LIAREA), Programa de Pós-Graduação em Computação Aplicada (PGCAP), Instituto Nacional de Pesquisas Espaciais (INPE) e-mail: dener.mendes@inpe.br, e-mail: valdivino.santiago@inpe.br

[2] Centro Federal de Educação Tecnológica de Minas Gerais e-mail: mateusangelo@cefetmg.br

Abstract. Open stellar clusters serve as fundamental probes for the comprehension of the stellar evolution and the Galactic structure. Traditional structural parameter estimation methods, such as Markov Chain Monte Carlo (MCMC), are computationally intensive and prone to local minima convergence. We propose BATEIA-1 (Balanced Astronomical Training for Estimation via Intelligent Approach), a scalable artificial intelligence driven approach. Crucially, this approach relies on a robust sampling strategy utilizing Gaia DR3 astrometric and photometric catalogueue to generate celestial maps. These maps feed nine Deep Neural Network (DNN) architectures for feature extraction, subsequently processed by Multilayer Perceptron (MLP) and Support Vector Regression (SVR) to determine analytical King profile parameters (central density, core, tidal radii and density background). This methodology circumvents optimization pitfalls, ensuring efficient automated characterization, with model interpretability validated via Grad-CAM.

Resumo. Aglomerados estelares abertos constituem ferramentas essenciais para a compreensão da evolução estelar e da estrutura galáctica. Métodos tradicionais de estimativa estrutural, como Markov Chain Monte Carlo (MCMC), apresentam alto custo computacional e suscetibilidade a mínimos locais. Propõe-se o BATEIA-1 (*Treinamento Astronômico Balanceado para Estimação via Abordagem Inteligente*), uma abordagem escalável baseado em inteligência artificial. A abordagem fundamenta-se em uma estratégia de amostragem robusta, utilizando dados astrométricos e fotométricos do catálogo Gaia DR3 para a geração de mapas celestes. Tais mapas alimentam nove arquiteturas de Redes Neurais Profundas (DNN) para extração de características, processadas posteriormente por Perceptrons Multicamadas (MLP) e Regressão de Vetores de Suporte (SVR) para determinar os parâmetros do perfil analítico de King (densidade central, raios de núcleo, de maré e densidade de fundo). A metodologia evita falhas de otimização, garantindo caracterização automatizada eficiente, com interpretabilidade validada via Grad-CAM.

Keywords. (Galaxy:) open clusters and associations: general – Galaxy: stellar content – Methods: data analysis

1. Introduction

Open clusters (OCs) are gravitationally bound systems that serve as tracers for the Galactic structure and stellar evolution. Their morphology is typically parameterized by the empirical King (1962) profile, defined by central density (σ_0), core radius (r_c), tidal radius (r_t), and background density (σ_{bg}). While the evolution of these parameters reflects internal relaxation and external tidal interactions, their determination via traditional methods involves constructing Radial Density Profiles (RDP). Techniques such as grid-based fitting, Markov Chain Monte Carlo (MCMC), or Maximum Likelihood estimation are statistically robust but computationally intensive and prone to local minima convergence.

To address these limitations, we propose the *Balanced Astronomical Training for Estimation via Intelligent Approach* (BATEIA-1)[1], a scalable approach utilizing artificial intelligence. A critical component of this methodology is the sampling strategy applied to astrometric and photometric data from the Gaia DR3 catalogue. Rather than processing tabular data directly, the system converts stellar distributions into pre-processed 512×512 pixel celestial maps, stripping all annotations to retain exclusively spatial information. These maps serve as input for feature extraction via pre-trained Deep Neural Networks (VGG, ResNet, DenseNet). Subsequently, Multilayer Perceptron (MLP) and Support Vector Regression (SVR) models map these features to the structural parameters. This data-driven approach automates the characterization of cluster architecture while maintaining physical interpretability, verified by means of Gradient-weighted Class Activation Mapping (Grad-CAM) (Selvaraju et al. 2020).

[1] The acronym is homonymous with the Portuguese term for a gold pan (from the Arabic *batiya*). Analogous to this instrument, which leverages density to segregate minerals from sediments, the proposed approach extracts visual features of clusters using their physics.

2. Sample and data

The dataset is composed of open star clusters spanning a comprehensive range of ages ($\log t \sim 6.7 - 9.6$), representing distinct evolutionary phases from early star formation to long-term dynamical relaxation. The fundamental parameters of the analyzed sample, categorized into young, intermediate, and old populations, are summarized in Table 1.

2.1. Pre-processing

The efficacy of the BATEIA-1 approach relies on a rigorous sampling and data preparation pipeline to generate high-fidelity celestial maps (Figure 1). Photometric and astrometric data were retrieved from the Gaia DR3 catalogue using ADQL queries with a cone search radius of $\sim 1^\circ - 2^\circ$ centered on the cluster coordinates. To ensure photometric completeness and data quality, the sample was restricted to magnitudes $G \leq 19$. Besides, in order to avoid sources with problematic astrometry and/or photometry, we also employed cuts (see Section 2 of Angelo et al. (2025)) considering the renormalized unit weight error parameter for as-

Table 1. Central coordinates, distances, and ages of the analyzed open clusters.

Cluster	RA [h:m:s]	DEC [°:′:″]	Dist. [kpc]	Age [log t]
Collinder277	15:04:21	-66:04:17	1.593 ± 0.003	8.975 ± 0.175
M67	12:50:52	11:48:54	0.837 ± 0.001	9.227 ± 0.179
NGC188	11:48:42	85:14:42	1.822 ± 0.003	9.42 ± 0.156
NGC581	23:20:16	60:39:13	2.527 ± 0.01	7.671 ± 0.192
NGC2516	23:30:07	-60:46:36	0.407 ± 0.0	8.098 ± 0.269
NGC3766	06:03:22	-61:36:42	1.939 ± 0.003	7.623 ± 0.2
NGC6531	07:02:31	-22:30:00	1.202 ± 0.003	6.735 ± 0.131
NGC6940	20:37:06	28:17:07	1.011 ± 0.001	8.886 ± 0.178
NGC7082	10:11:22	47:06:13	1.321 ± 0.002	8.166 ± 0.217
Ruprecht91	17:56:19	-57:29:41	1.031 ± 0.001	8.172 ± 0.222
NGC6811	06:20:27	46:22:43	1.11 ± 0.001	9.032 ± 0.183
Berkeley98	04:39:28	52:24:40	3.643 ± 0.029	9.086 ± 0.172
Haffner13	19:13:34	-30:02:52	0.552 ± 0.0	7.165 ± 0.243
NGC129	07:36:27	60:12:44	1.789 ± 0.003	8.021 ± 0.197
NGC2266	04:49:55	26:58:35	3.354 ± 0.027	8.902 ± 0.211
NGC2422	18:08:57	-14:30:15	0.468 ± 0.0	8.036 ± 0.246
NGC2425	18:34:36	-14:53:32	3.094 ± 0.022	9.296 ± 0.161
NGC3960	09:39:06	-55:40:40	2.208 ± 0.006	8.908 ± 0.166
Ruprecht171	14:00:51	-16:03:59	1.482 ± 0.003	9.168 ± 0.167
NGC6791	02:13:12	37:46:40	4.189 ± 0.019	9.58 ± 0.163

trometry (RUWE, Lindegren et al. (2021)) and the corrected flux excess factor parameter for photometry (E(BP/RP), Evans et al. (2018)).

To mitigate field star contamination, which degrades the contrast of the cluster features in the input images, a kinematic filter was applied. For each cluster, a Vector-Point Diagram (VPD) of proper motions was constructed to identify the centroid of the member population. A box-shaped filter was subsequently applied to retain only stars with proper motions consistent with the cluster's kinematic signature. The size of the proper motion filters is at least 3 times the intrinsic dispersion of μ^*_{alpha} and mu_δ inferred from member stars, as published in (Angelo et al. 2023) and (Angelo et al. 2025).

2.2. Coordinate transformation

To generate the projected density maps required for the DNNs, the equatorial coordinates (α, δ) of the proper-motion filtered samples were transformed into a Cartesian plane (X, Y) tangent to the cluster centre (α_c, δ_c). Following the projection relations by van de Ven et al. (2006), the coordinates are given by:

$$X = r_0 \cos\delta \cdot \sin(\alpha - \alpha_c), \tag{1}$$

$$Y = r_0 \left[\sin\delta \cdot \cos\delta_c - \sin\delta_c \cdot \cos\delta \cdot \cos(\alpha - \alpha_c)\right], \tag{2}$$

where $r_0 = 180/\pi$ converts the result to degrees. This transformation places the cluster center at the origin $(0, 0)$ and establishes a Euclidean metric where the radial distance is defined as $r = \sqrt{X^2 + Y^2}$. The resulting spatial distributions form the basis for the pre-processed celestial maps utilized in the subsequent feature extraction phase.

3. Methodology

The BATEIA-1 approach infers structural parameters directly from stellar spatial distributions, bypassing the iterative construction of the RDP's during inference. The methodology connects the extraction of visual features from celestial maps to the regression of physical parameters defined by the King profile.

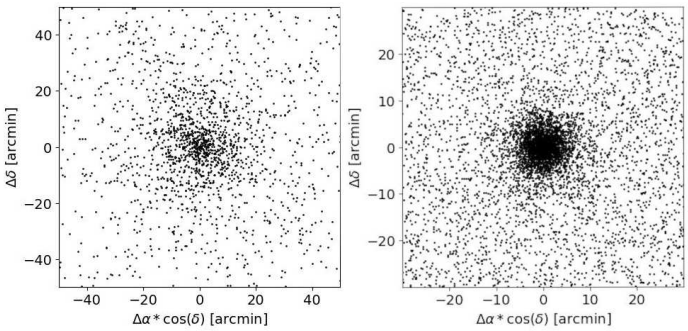

Figure 1. Representative pre-processed celestial maps generated after kinematic filtering and coordinate transformation: NGC 6791 (left) and M67 (right).

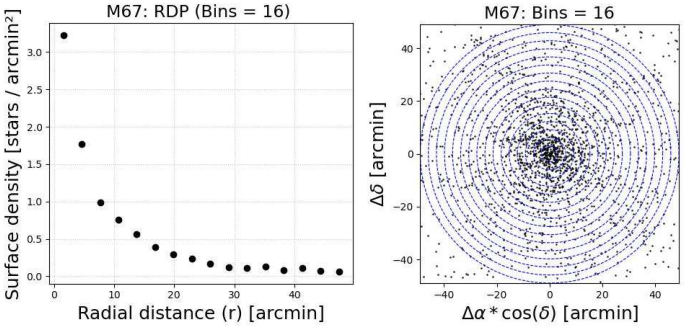

Figure 2. M67: *RDP* for the topology with the lowest residuals (left) and binning of the topology with the lowest residuals (right).

3.1. Sampling

To establish reliable reference labels for the Deep Neural Networks (DNNs), we implemented a systematic sampling procedure based on the analysis of RDP's. This process defines the structural parameters $(\sigma_0, r_c, r_t, \sigma_{bg})$ by fitting the King analytical profile to observed stellar distributions. While the methodology was applied to the full dataset of twenty clusters, M67 is used herein for illustrative purposes.

3.1.1. Radial Density Profile (RDP) Construction

For each star, the radial distance r from the cluster center $(0, 0)$ is computed in arcminutes (Eq. 3) using the projected Cartesian coordinates described in Section 2.2.

$$r = \left(\sqrt{(X - x_{\text{center}})^2 + (Y - y_{\text{center}})^2}\right) \times 60. \tag{3}$$

The RDP is constructed by partitioning the spatial domain into concentric annuli (bins) up to a maximum radius $r_{\max}$. The stellar density within each bin is calculated as the ratio of star counts to the ring area. To ensure the robustness of the sampling, we generated 36 distinct topologies for each cluster, incrementally varying the resolution from 5 to 40 radial divisions.

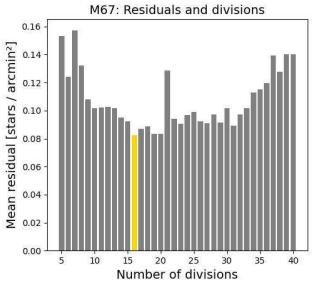

Figure 3. M67: Residuals for each topology

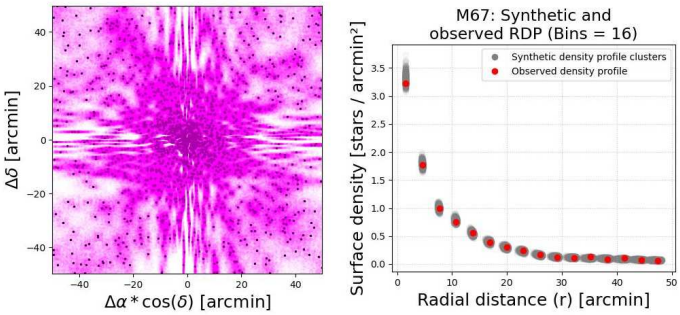

Figure 4. M67: Real and synthetic clusters overview (left) and *RDP* comparison for real and synthetic data (right).

3.1.2. King profile fitting and topology selection

The structural parameters are derived by fitting the King empirical law (Eq. 4) to the calculated RDPs:

$$\sigma(r) = \sigma_0 \left(\frac{1}{\sqrt{1 + \left(\frac{r}{r_c}\right)^2}} - \frac{1}{\sqrt{1 + \left(\frac{r_t}{r_c}\right)^2}} \right)^2 + \sigma_{bg}, \quad (4)$$

where σ_0, r_c, r_t, and σ_{bg} represent the central density, core radius, tidal radius, and background density, respectively. To determine the sampling topology, residuals were calculated relative to reference parameters from Angelo et al. (2025) and **?**. The parameters obtained from the configuration minimizing these residuals serve as input for the regressors (3.3).

Since the discretization of the RDP influences the parameter estimation, the optimal sampling topology was selected via residual minimization. For each of the 36 configurations, we computed the residuals between the observed density and the King model. The topology yielding the lowest residuals was adopted as the representative configuration (Figure 3). The parameters derived from this optimized topology serve as the ground truth targets for training the DNNs.

3.2. Data augmentation and synthetic generation

The dataset consists of 20,000 images, derived from 1,000 synthetic instances generated for each of the 20 real clusters. These instances are stratified into four equal subsets of 250 samples, with maximum displacement ranges of 10%, 20%, 30%, and 40%, respectively.

This synthetic generation provides a controlled environment to train the Deep Neural Networks (DNNs), bridging the gap between limited observational data and the requirements of deep learning.

The augmentation process applies random perturbations to the projected Cartesian coordinates (X, Y) of the stars, stratified into four subsets with increasing displacement magnitudes. This strategy systematically introduces noise while preserving the underlying cluster structure.

To maintain spatial coherence, a reflection boundary condition is enforced: any coordinate perturbation exceeding the maximum radius $r_{\max}$ is reflected back into the valid domain. Crucially, the synthetic clusters retain the specific sampling topology (binning configuration) of their parent real cluster (Figure 4). This ensures that the model learns to interpret physical parameter variations manifested as vertical shifts in density values, rather than artifacts of the spatial grid.

3.3. Dense Neural Network (DNN)

The BATEIA-1 approach relies on deep feature representations derived from artificial photographs depicting the spatial distribution of stars. Feature extraction is performed by three pre-trained DNN families—VGG Simonyan & Zisserman (2014), DenseNet Huang et al. (2017), and ResNet He et al. (2016)—initialized on the ImageNet-1K dataset. To standardize the output for regression, Global Average Pooling (GAP) is applied to the final convolutional layers, generating fixed-length feature vectors ranging from 512 to 2208 dimensions.

The feature vectors serve as input for a MLP (**?**) and a SVR (Drucker et al. 1997), implemented in PyTorch (Paszke et al. 2019) and Scikit-learn (Pedregosa et al. 2011), respectively. Both models utilize the AdamW algorithm (Loshchilov & Hutter 2019), with hyperparameters tuned via Optuna (Akiba et al. 2019). The evaluation employs a global shuffling strategy, partitioning the dataset into 70% for training and validation and 30% for testing, independent of cluster origin, to estimate the structural parameters $(\sigma_0, r_c, r_t, \sigma_{\rm bg})$

4. Results

The effectiveness of the suggested sampling and data augmentation techniques in encoding astrophysical information into deep representations is confirmed by the BATEIA-1 approach's performance evaluation. This section assesses the BATEIA-1 approach, specifically validating the efficacy of the proposed sampling strategy in encoding physical properties into visual features. The evaluation combines quantitative metrics with Explainable AI (XAI) to confirm that the data treatment pipeline—encompassing coordinate projection, RDP-based topology selection, and synthetic augmentation—preserved the morphological fidelity required for accurate inference. Experiments were conducted on an NVIDIA RTX A4000 workstation.

4.1. Physical validation and interpretability

Explainable Artificial Intelligence (XAI) methods were first used to confirm the sampling procedure dependability. We verified that the pre-processed celestial maps provide enough morphological signal for physical characterisation by applying Score-CAM and Ablation-CAM to the feature extraction layers. The produced heatmaps (Figure 5) show that the DNNs concentrate on physically significant structures: the field periphery and transition zones determine the background density (σ_{bg}) and tidal radii (r_t), while the core regions are given priority for estimating central density (σ_0).

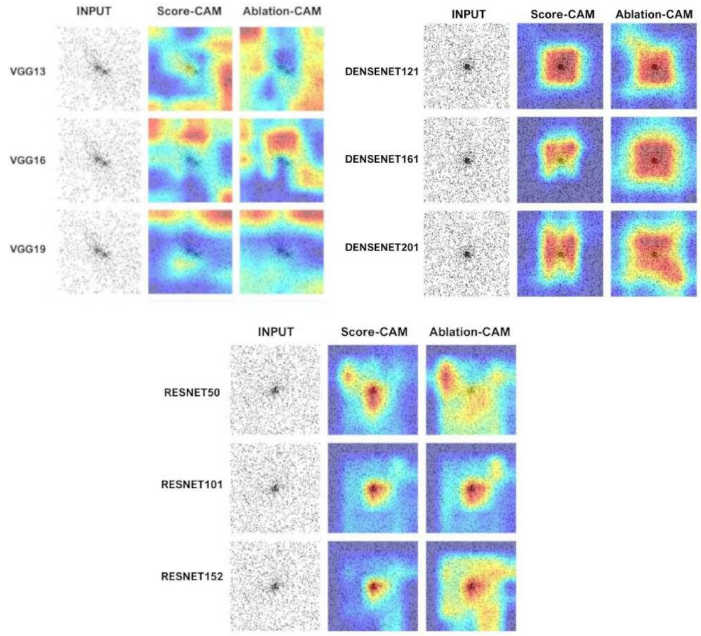

Figure 5. Activation heatmaps for different architectures: Haffner 13 using VGG family (left), Berkeley 98 using ResNet family (center) and NGC 2266 using DenseNet family (right).

Table 2. Comparison of central density (σ_0) values [stars/arcmin^2] for a representative subset.

Cluster	σ_0 [stars/arcmin^2]		
	Angelo et al. (2025)	Hunt et al. (2024)	BATEIA-1
Collinder277	2.07 ± 0.30	1.72	2.12 ± 0.31
M67	4.15 ± 0.40	1.65	4.11 ± 0.39
Berkeley98	8.68 ± 1.50	8.34	8.95 ± 1.55
Haffner13	0.36 ± 0.05	0.22	0.32 ± 0.05
NGC129	4.52 ± 0.50	3.94	4.57 ± 0.51

This visual congruence implies that the coordinate transformation and kinematic filtering steps (Section 2.2) successfully isolated the cluster morphology from noise, enabling the extractors to distinguish between member stars and field contamination without reliance on spurious artifacts.

4.2. Benchmark setting

The quantitative assessment, conducted under the *benchmark setting* via global data shuffling, validates the synthetic generation strategy. The observed low residual errors across the dynamic range confirm the consistency of ground truth labels derived from optimized King fit topologies. While performance was verified for the complete dataset of twenty clusters, the following tables present a representative subset of five morphologically distinct objects. These cases reflect the accuracy observed for the entire sample, demonstrating the model's capacity to recover parameters spanning multiple orders of magnitude.

For central density (σ_0), predictions ranged accurately from sparse systems like Haffner 13 (~ 0.32 stars/arcmin^2) to denser cores like Berkeley 98 (~ 8.95 stars/arcmin^2), as shown in Table 2. This indicates that the chosen spatial resolution of the input maps (512×512) preserves sufficient granularity to resolve density peaks without saturation. The scatter plot presented in Figure 6 illustrates the high correlation between predicted and reference values for the first synthetic subset (Group 1), a performance pattern that is consistently observed across all generated groups.

Table 3. Comparison of core radius (r_c) values [arcmin] for a representative subset.

Cluster	r_c [arcmin]		
	Angelo et al. (2025)	Hunt et al. (2024)	BATEIA-1
Collinder277	4.8 ± 0.8	5.7	4.74 ± 0.79
M67	7.3 ± 0.94	10.85	7.14 ± 0.91
Berkeley98	1.8 ± 0.4	1.29	1.84 ± 0.41
Haffner13	17.7 ± 2.58	22.03	17.94 ± 2.62
NGC129	6.1 ± 1.5	4.96	6.37 ± 1.57

Table 4. Comparison of tidal radius (r_t) values [arcmin] for a representative subset.

Cluster	r_t [arcmin]		
	Angelo et al. (2025)	Hunt et al. (2024)	BATEIA-1
Collinder277	25.8 ± 7.78	19.64	25.68 ± 7.73
M67	45.5 ± 11.75	35.76	44.78 ± 11.55
Berkeley98	23.1 ± 9.2	26.97	19.08 ± 7.6
Haffner13	85.6 ± 23.73	71.01	84.3 ± 23.35
NGC129	21.6 ± 2.69	30.89	20.57 ± 2.57

Table 5. Summary of the best-performing architectures for the Benchmark strategy.

Parameter	Best combination	Avg. Error (%)
σ_0	DENSENET121 + BMMLP	1.6520
r_c	RESNET152 + BMSVR	1.3766
r_t	VGG19 + BMSVR	5.0710
σ_{bg}	VGG19 + BMSVR	0.2726

Similarly, the inference of core (r_c) and tidal radii (r_t) validated the data augmentation method, specifically the reflection boundary condition, which prevented edge artifacts in the synthetic samples. The model correctly differentiated between compact objects like Berkeley 98 ($r_t \approx 19.08$ arcmin) and extensive systems like Haffner 13 ($r_t \approx 84.3$ arcmin). As evidenced by the representative plots in Figure 6, the BATEIA-1 predictions align closely with the literature estimates, confirming that the structural dimensions are correctly inferred regardless of the displacement levels applied during sampling.

Regarding the background density (σ_{bg}), the results confirm that the kinematic filtering applied during sampling (based on proper motion VPDs) effectively enhanced the cluster-to-field contrast. The model accurately quantified sparse backgrounds (e.g., Haffner 13) and denser fields. Figure 6 displays the regression results for Group 1, which are indicative of the overall system performance, demonstrating close agreement with literature values in all analyzed scenarios.

Table 5 summarizes the optimal architectures, revealing that feature extraction performance is closely tied to spatial sampling properties: ResNet152 excels at high-frequency central details, while VGG19 is more robust for low-density peripheral gradients.

5. Final remarks

The BATEIA-1 approach presents a methodology for determining the structural parameters of open clusters by integrating the analytical King profile with deep learning techniques. The generation of synthetic variations based on optimized RDP topologies allowed the networks to encode physical morphological features rather than specific image artifacts. This result indicates that the sampling protocol bridged the domain gap between synthetic

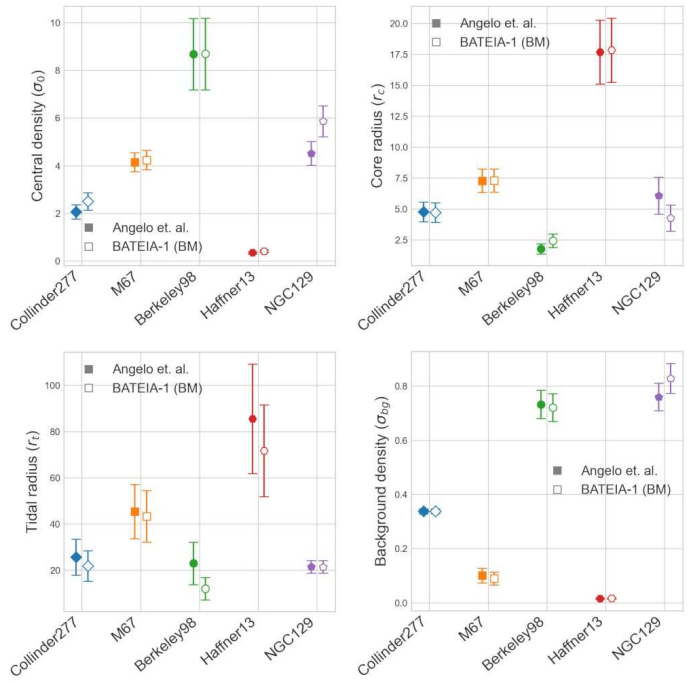

Figure 6. Correlations between predicted and reference values for the Group 1 synthetic subset across all structural parameters: σ_0 (top left), r_c (top right), r_t (bottom left), and σ_{bg} (bottom right).

representations and observational data from the Gaia DR3 catalogue.

Methodologically, the application of Global Average Pooling (GAP) standardized feature vectors across distinct architectures (VGG, ResNet, DenseNet). Explainable AI (XAI) analysis indicated that these architectures activate on distinct spatial frequencies: ResNet focuses on core regions, associated with σ_0 and r_c, while DenseNet utilizes a broader receptive field to identify tidal boundaries (r_t) and background levels (σ_{bg}).

Regarding computational efficiency, the training phase concentrates the processing load, with the SVR requiring approximately 85% more time than the MLP. However, the pre-trained library allows for millisecond-latency inference, compatible with the processing requirements of large-scale surveys.

Acknowledgements. This research was developed within the *Laboratório de Inteligência ARtificial para Aplicações AeroEspaciais e Ambientais* (LIAREA) related to the project *Classificação de imagens e dados via redes neurais profundas para múltiplos domínios* (Image and data classification via Deep neural networks for multiple domainS — IDeepS). The IDeepS (available online: https://github.com/vsantjr/IDeepS (accessed on 28 July 2025)) project is supported by the *Laboratório Nacional de Computação Científica* (LNCC, MCTI, Brazil) via resources of the SDumont supercomputer. This study was financed in part by the Coordenação de Aperfeiçoamento de Pessoal de Nível Superior - Brasil (CAPES) – Finance Code 001, grant 88887.958398/2024-00. This research has made use of the VizieR catalogueue access tool, CDS, Strasbourg, France. This research has made use of the SIMBAD database, operated at CDS, Strasbourg, France. This work has made use of data from the European Space Agency (ESA) mission Gaia (https: //www.cosmos.esa.int/gaia), processed by the Gaia Data Processing and Analysis Consortium (DPAC, https://www.cosmos.esa.int/web /gaia/dpac/consortium). Funding for the DPAC has been provided by national institutions, in particular the institutions participating in the Gaia Multilateral Agreement. This research has made use of Aladin sky atlas developed at CDS, Strasbourg Observatory, France. This research has made use of the WEBDA database, operated at the Department of Theoretical Physics and Astrophysics of the Masaryk University

References

Abraham, B. & Ledolter, J. 2009, Statistical methods for forecasting (John Wiley & Sons)
Akiba, T., Sano, S., Yanase, T., Ohta, T. & Koyama, M. 2019, Proc. KDD, 2623
Angelo, M. S., Santos Jr, J. F. C., Maia, F. F. S. & Corradi, W. J. B. 2023, MNRAS, 522, 956
Angelo, M. S., Santos, J. F. C., Corradi, W. J. B. & Maia, F. F. S. 2025, MNRAS, 539, 2513
Bengio, Y. et al. 2009, Found. Trends Mach. Learn., 2, 1
Binney, J. & Tremaine, S. 1998, Galactic Dynamics (Princeton Univ. Press)
Bisht, D., Zhu, Q., Yadav, R. K. S., Durgapal, A. & Rangwal, G. 2020, MNRAS, 494, 607
Çakmak, H. et al. 2024, Astron. Nachr., e20240054
de La Fuente Marcos, R. 1997, A&A, 322, 764
Dias, W. S. et al. 2021, MNRAS, 504, 356
Ding, X. et al. 2021, PASJ, 73, 1486
Drucker, H. et al. 1997, NeurIPS, 9, 155
Ester, M., Kriegel, H.-P., Sander, J. & Xu, X. 1996, Proc. KDD, 96, 226
Evans, D. W. et al. 2018, A&A, 616, A4
Feigelson, E. D. & Babu, G. J. 2012, arXiv:1205.2064
Feng, Z., Zhu, M., Stanković, L. & Ji, H. 2021, Remote Sens., 13, 1772
Fisher, R. A. 1925, Statistical methods for research workers (Edinburgh: Oliver and Boyd)
Foreman-Mackey, D., Hogg, D. W., Lang, D. & Goodman, J. 2013, PASP, 125, 306
Geyer, M. P. & Burkert, A. 2001, MNRAS, 323, 988
Gieles, M. & Baumgardt, H. 2008, MNRAS, 389, L28
Goodwin, S. P. 1997, MNRAS, 284, 785
Gratton, R. et al. 2019, A&A Rev., 27, 8
Guidotti, R. et al. 2018, ACM Comput. Surv., 51, 1
Harris, W. E. & Racine, R. 1979, ARA&A, 17, 241
Hassija, V. et al. 2024, Cogn. Comput., 16, 45
He, K., Zhang, X., Ren, S. & Sun, J. 2016, CVPR, 770
Hills, J. G. 1980, ApJ, 235, 986
Huang, G., Liu, Z., Van Der Maaten, L. & Weinberger, K. Q. 2017, CVPR, 4700
Hunt, E. L. & Reffert, S. 2024, A&A, 686, A42
Hyndman, R. J. & Koehler, A. B. 2006, Int. J. Forecast., 22, 679
King, I. 1962, AJ, 67, 471
Lada, C. J. & Lada, E. A. 2003, ARA&A, 41, 57
LeCun, Y., Bottou, L., Bengio, Y. & Haffner, P. 1998, Proc. IEEE, 86, 2278
Lin, M., Chen, Q. & Yan, S. 2013, arXiv:1312.4400
Lindegren, L. et al. 2021, A&A, 649, A2
Lindoff, U. 1972, A&A, 16, 315
Loshchilov, I. & Hutter, F. 2019, ICLR
Maia, F. F. S. 2012, PhD Thesis, Univ. Federal de Minas Gerais
McKee, C. F. & Ostriker, E. C. 2007, ARA&A, 45, 565
Meylan, G. & Heggie, D. C. 1997, A&A Rev., 8, 1
Netopil, M., Paunzen, E., Heiter, U. & Soubiran, C. 2016, A&A, 585, A150
Paszke, A. et al. 2019, NeurIPS, 32, 8024
Pavani, D. B. & Bica, E. 2007, A&A, 468, 139
Pedregosa, F. et al. 2011, JMLR, 12, 2825
Piatti, A. E., Dias, W. S. & Sampedro, L. M. 2017, MNRAS, 466, 392
Piskunov, A. E. et al. 2007, A&A, 468, 151
Portegies Zwart, S. F., McMillan, S. L. A. & Gieles, M. 2010, ARA&A, 48, 431
Prisinzano, L., Micela, G., Sciortino, S. & Favata, F. 2003, A&A, 404, 927
Ramaswamy, H. G. et al. 2020, WACV, 983
Renaud, F., Gieles, M. & Boily, C. M. 2011, MNRAS, 418, 759
Rumelhart, D. E., Hinton, G. E. & Williams, R. J. 1986, Nature, 323, 533
Saraiva, M. F. O. 2004, Astronomia & Astrofísica (Ed. Livraria da Física)
Selvaraju, R. R. et al. 2020, IJCV, 128, 336
Simonyan, K. & Zisserman, A. 2014, arXiv:1409.1556
Smola, A. J. & Schölkopf, B. 2004, Stat. Comput., 14, 199
Tarricq, Y. et al. 2022, A&A, 659, A59
Vallenari, A. et al. (Gaia Collaboration) 2023, A&A, 674, A1
van de Ven, G., van der Marel, R. P., Rix, H.-W. & Cappellari, M. 2006, A&A, 445, 513
Vandersmissen, B. & Oramas, J. 2024, CVIU, 241, 103934
Wang, H. et al. 2020, CVPR Workshops, 24